Organ registration in augmented surgery from an optimal control perspective

Stéphane Cotin, Guillaume Mestdagh, Yannick Privat

Organ registration in augmented surgery from an optimal control perspective

Stéphane Cotin* [1], Guillaume Mestdagh † [1,2], and Yannick Privat ‡ [1,2,3]

[1]Inria, Strasbourg, France.
[2]IRMA, Université de Strasbourg, CNRS UMR 7501, 7 rue René Descartes, 67084 Strasbourg, France.
[3]Institut Universitaire de France (IUF).

March 22, 2023

Abstract

We address the problem of organ registration in augmented surgery, where the deformation of the patient's organ is reconstructed in real-time from a partial observation of its surface. Physics-based registration methods rely on adding artificial forces to drive the registration, which may result in implausible displacement fields. In this paper, we look at this inverse problem through the lens of optimal control, in an attempt to reconstruct a physically consistent surface load. The resulting optimization problem features an elastic model, a least-squares data attachment term based on orthogonal projections, and an admissible set of surface loads defined prior to reconstruction in the mechanical model. After a discussion about the existence of solutions, we analyze the necessary optimality conditions and use them to derive a suitable optimization algorithm. We implement an adjoint method and we test our approach on multiple examples, including the so-called *Sparse Data Challenge*. We obtain very promising results, that illustrate the feasibility of our approach with linear and nonlinear models.

Keywords: Shape registration, Augmented Surgery, Optimal Control

1 Introduction

Compared to open surgery, minimally-invasive surgery is known to improve the outcome of surgical interventions, reducing pain and infection risk. During a minimally-invasive operation, the surgeon manipulates organs using instruments inserted through small incisions in the patient's abdomen. They receive visual feedback on a screen, thanks to a laparoscopic camera inserted through one of the incisions. In this context of indirect interaction and feedback, operations such as tumor resection remain challenging. The surgeon must navigate in an opaque organ, avoiding blood vessels and following the motion due to breathing and heartbeats.

Augmented reality systems have been designed to help the medical staff visualize the motion of the organ internal structures, including tumours and blood vessels. An example in hepatic surgery is given in [22]. The augmented reality pipeline features an elastic registration procedure, which combines data acquired before and during the intervention. Namely, an initial liver mesh is segmented from tomographic images made before the operation. As the intervention goes on, a point cloud, representing

*stephane.cotin@inria.fr
†guillaume.mestdagh@inria.fr
‡yannick.privat@unistra.fr

the liver surface as it appears in the camera field of view, is provided in real time. The registration procedure deforms the pre-operative liver model so that its surface matches the observed point cloud.

The elastic registration problem raises several challenges. First, the deformed view should be updated in real time along the intervention. Though we do not pretend to achieve real-time registration in this paper, we keep in mind that numerical methods should be as simple as possible. In addition, intra-operative data only show a part of the current organ surface. As a consequence, many solutions to the matching problem exist, most of which are not consistent with the physics of the problem. A successful registration approach should reduce as much as possible the range of reachable displacements, to return a displacement field as close as possible to the true organ displacement.

Numerous elastic registration methods are nonrigid variants of the Iterative Closest Point algorithm [3]. They are inspired from image registration methods [47, Section II.A.1], where a cost function is minimized to enforce landmark correspondence, while the elastic energy is used as a penalty term to regularize the displacement field. In these methods, fictitious forces are introduced into the direct model to drive the registration. Artificial forces applied to the organ surface include electrostatic forces [48], linear and nonlinear springs [21, 43], or Lagrange multipliers that enforce a so-called sliding constraint between the deformed surface and the observed point cloud [41, 9, 33].

Such methods rely on elaborate constitutive laws, where attention is paid to the stress-strain law [28], additional stiffness due to blood vessels [42, 21], and boundary conditions [40, 36]. Unfortunately, whether they derive from an imaginary potential or play the role of constraint-enforcing Lagrange multipliers, the forces driving the registration do not reflect the real causes of displacement. They are created by the intra-operative point cloud, which does not really exist. This results in unrealistic displacement fields, regardless of the elastic model accuracy [45]. Several methods prefer to solve an inverse problem, where a range of admissible deformations is defined based on physical hypotheses. Using linear elasticity, the authors in [23, 24] precompute a basis of displacements corresponding to forces applied in zones where ligaments hold the liver, while they impose a free boundary condition on the remaining surface. In [39], the initial liver pose is estimated by taking into account the effects of gravity and gas insufflation in the patient's abdomen. In [49], forces that create the displacement are restricted to certain nodes of the liver mesh. Approaches based on an inverse problem often exhibit an improved registration accuracy and produce more physically relevant displacement fields, at the expense of execution time.

In this paper, we look at the registration inverse problem from the perspective of optimal control. While most registration methods are very specific to a given registration scenario, expressed in terms of finite-dimensional matrix-vector operations, and, often tailored for linear elasticity, we take a step backward and consider the continuous problem in a more general setting. Using the optimal control framework results in a very flexible formulation, yielding at the same time physically relevant displacement fields, and where it is easy to include new physical hypotheses or take additional intra-operative data into account. The wide range of tools provided by the optimal control framework may be of help to obtain precious mathematical insight about the registration problem. Last but not least, we expect our approach to lead to new numerical methods inspired from generic numerical optimization algorithms. The optimal control approach problem studied in this problem was already introduced in our conference paper [30], which includes numerical examples associated to the augmented surgery domain.

In the remaining of this paper, we begin by stating the physical model, along with the optimization problem we consider (Section 2). Then, we propose a mathematical analysis of the optimal control problem, including the existence of solutions and optimality conditions (Section 3). Finally, we show some numerical tests to evaluate the performances of our approach (Section 4).

2 Towards an optimal control formulation

In our approach, we determine a surface force distribution on the organ boundary that generates a displacement compatible with observed data. The reconstructed force distribution is chosen among a set of admissible force distributions, which reflects a range of physical causes. Of course, we do not expect the registration procedure to accurately estimate the forces that created the observed deformation. The formulation we propose nevertheless allows us to get close to the physics of the problem in a satisfactory way, while leading to efficient algorithmic methods that are easy to implement. We illustrate our approach with physical examples.

2.1 Pre-operative biomechanical model

Figure 1 shows a sketch of the system we consider. In its reference configuration, the organ is represented by an open domain $\Omega_0 \subset \mathbb{R}^3$ with Lipschitz boundary, filled with an elastic material. Due to its interactions with its environment, the organ is subject to surface loadings, such as pressure or contact with surrounding tissues. Volume forces, such as gravity, are not considered in this study. The boundary $\partial\Omega_0$ falls into two parts, $\partial\Omega_{\mathrm{D}}$ and $\partial\Omega_{\mathrm{N}}$. On $\partial\Omega_{\mathrm{D}}$, a homogeneous Dirichlet boundary condition applies, whereas the Neumann boundary $\partial\Omega_{\mathrm{N}}$ is subject to a surface force distribution $g \in L^2(\partial\Omega_{\mathrm{N}}, \mathbb{R}^3)$. A homogeneous Dirichlet boundary condition is typically set in zones where main blood vessels enter the organ. The space of displacement fields associated with this partition reads

$$H^1_{\mathrm{D}}(\Omega_0) = H^1_{\mathrm{D}}(\Omega_0, \mathbb{R}^3) = \left\{ u \in H^1(\Omega_0, \mathbb{R}^3) \;\middle|\; u = 0 \text{ on } \partial\Omega_{\mathrm{D}} \right\},$$

and we denote by $u_g \in H^1_{\mathrm{D}}(\Omega_0)$ the displacement field generated by a given surface force distribution g on $\partial\Omega_N$.

Elastic stress-strain laws used in the literature to describe the behaviour of living tissues range from the linear elastic model [23] to hyperelastic models such as Neo-Hookean [31] or Ogden [36] models (see also [28] and references therein). When computation time is a constraint, the linear co-rotational model is sometimes preferred [35, 43], as it generates nonlinear deformations at the cost of a linear system inversion. In this paper, we only consider the linear elastic system, except for a brief nonlinear example in the results section. In the linear case, the generated displacement u_g solves the partial differential equation (PDE)

$$\begin{cases} \operatorname{div}(A\varepsilon(u)) &= 0 \quad \text{in } \Omega_0 \\ u &= 0 \quad \text{on } \partial\Omega_{\mathrm{D}} \\ A\varepsilon(u)\cdot n &= g \quad \text{on } \partial\Omega_{\mathrm{N}}, \end{cases} \tag{1}$$

where the linearized strain tensor and the Hooke tensor are defined by

$$\varepsilon(u) = \tfrac{1}{2}\left(\nabla u + \nabla u^{\mathrm{T}}\right) \quad \text{and} \quad A\varepsilon = 2\mu\varepsilon + \lambda \operatorname{tr}(\varepsilon) I,$$

respectively. The Lamé parameters μ and λ describe the material resistance to deformation and volume change. They are defined from the Young modulus E and the Poisson ratio ν by $\mu = E/(2(1+\nu))$ and $\lambda = 2\nu\mu/(1-2\nu)$.

We denote by $\Omega_u = (\mathrm{Id}+u)(\Omega_0)$ the volume occupied by the deformed organ. Note that we do not expect $(\mathrm{Id}+u)$ to be a bijection, which is consistent with our numerical framework.

2.2 Intra-operative data and surface-matching functional

While the reference configuration Ω_0 is known through pre-operative images, the current position shall be estimated from an intra-operative observation. In our continuous model, the observed data take the form of a compact two-dimensional surface $\Gamma \subset \mathbb{R}^3$. We denote by $S_0 \subset \partial\Omega_0$ the part of the initial organ boundary that is supposed to match with Γ as the registration ends. We assume that S_0 is a

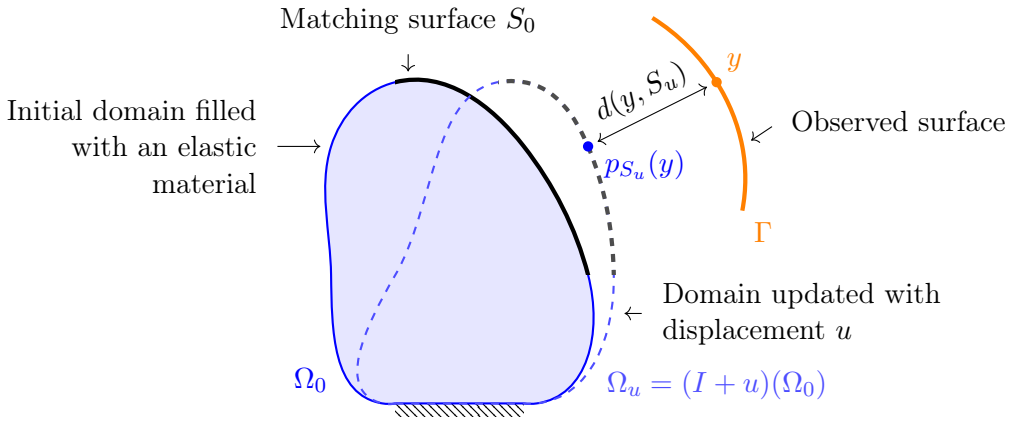

Figure 1: Problem geometry. The thick dashed line represents the deformed matching surface S_u. The distance between a point $y \in \Gamma$ and its orthogonal projection onto S_u is denoted by $d(y, S_u)$.

compact subset of $\partial\Omega_0$ known by the user (possibly the whole boundary $\partial\Omega_0$), and we will use the notation

$$S_u = (\mathrm{Id} + u)(S_0) \subset (\mathrm{Id} + u)(\partial\Omega_0)$$

to denote the image of S_0 under a displacement u. The surface S_0 is chosen before the operation starts, as the surgeon has a vague idea of what part of the organ boundary should appear on the camera.

To measure the discrepancy between a given displacement and the observed data, we introduce the least-squares function $J : C(\overline{\Omega}_0) \to \mathbb{R}$, defined by

$$J(u) = \tfrac{1}{2} \int_\Gamma d^2(y, S_u)\, \mathrm{d}y, \tag{2}$$

where $d(y, S_u)^2 = \min_{x \in S_u} \|x - y\|^2$ denote the Euclidean distance between $y \in \Gamma$ and S_u. Therefore, $J(u)$ vanishes whenever $\Gamma \subset S_u$, up to a zero Lebesgue measure set. Existing approaches in shape-matching use shape similarity metrics between sets such as the signed distance with respect to the target [11, 34] or the Hausdorff distance [38]. However, they are not relevant in this case, as we are not comparing shapes, but only open surfaces. Following previous approaches in partial shape-matching [45, 41], we fall back to the least-squares functional (2). The approaches described in these aforementioned references differ from the one described in this article in the sense that they depend on a particular choice of discretization and meshing of the problem. Our approach, on the other hand, is robust to a change of such parameters.

We consider the constrained optimization problem

$$\min_{g \in \mathcal{G}_M} \Phi(g) \quad \text{where} \quad \Phi(g) = J(u_g), \tag{3}$$

where the feasible set reads

$$\mathcal{G}_M = \left\{ g \in L^\infty(\partial\Omega_\mathrm{N}, \mathbb{R}^3) \;\middle|\; \|g\|_{L^\infty(\partial\Omega_\mathrm{N})} < M \right\}.$$

Here, the definition of $\mathcal{G}_M$ is based on the physical hypothesis that the magnitude of surfaces forces that are expected in the human body does not exceed the positive constant $M > 0$. Note that, in our numerical examples, the definition of admissible forces also includes information concerning the support of g, i.e. the zones where surface forces apply on the organ boundary.

Setting an upper bound on the pointwise magnitude of g is also useful to handle noise in the observed surface Γ. In the medical application, Γ is a point cloud provided by an image processing pipeline. It is likely to include a certain level of noise. In this context, an exact matching between Γ and the

organ boundary would result in a very irregular displacement field and oscillations in the surface force distributions. A better outcome would consist in the organ boundary passing through the point cloud without meeting every point individually. Using the constraint prevents the control g from taking the large values it needs to reach every point in Γ.

3 Analysis of the optimal control problem

To begin with, an analysis of the optimization problem should help us obtain some mathematical insight. After we discuss the existence of solutions to the continuous problem, we derive first-order optimality conditions. Optimality conditions will be useful when it comes to implementing a numerical method to solve the problem in silico. We take care of that part in the end of the section.

For $q > 0$, we introduce the notation $W^{1,q}_{\mathrm{D}}(\Omega_0, \mathbb{R}^3)$ to denote the Sobolev space

$$W^{1,q}_{\mathrm{D}}(\Omega_0, \mathbb{R}^3) = \left\{ u \in W^{1,q}(\Omega_0, \mathbb{R}^3) \;\middle|\; u = 0 \text{ on } \partial\Omega_{\mathrm{D}} \right\},$$

and $q' > 0$ is the conjugate exponent to q, given by $1/q + 1/q' = 1$. Then, the topological dual of $W^{1,q'}_{\mathrm{D}}(\Omega_0, \mathbb{R}^3)$ with respect to the pivot space $L^2(\Omega_0, \mathbb{R}^3)$ is denoted by $W^{-1,q}_{\mathrm{D}}(\Omega_0, \mathbb{R}^3)$.

3.1 Well-posedness

Existence of solutions for Problem (3) is critical to guarantee the stability properties of the discrete problem with respect to the mesh size, or which regularity can be be expected for numerical solutions.

The following results are based on the work by Gröger [16] around the regularity of solutions to partial differential equations with mixed boundary conditions. The definition of a Gröger-regular set is based on the following subsets of $\mathbb{R}^3$:

$$B = \{x \in \mathbb{R}^3 \mid \|x\| < 1\}, \quad B_+ = \{x \in B \mid x_3 > 0\}, \quad D = \{x \in B \mid x_3 = 0\}, \quad D_0 = \{x \in D \mid x_1 < 0\}.$$

Definition 3.1. *Let Ω_0 a bounded open subset of $\mathbb{R}^3$ and $\partial\Omega_{\mathrm{N}}$ a relatively open part of its boundary. The set $G = \Omega_0 \cup \partial\Omega_{\mathrm{N}}$ is said to be regular in the sense of Gröger if, for each $x \in \partial\Omega_0$, there is a neighbourhood U of x and a Lipschitz diffeomorphism $\Psi : U \to B$ such that $\Psi(U \cap G)$ either coincides with B_+, or $B_+ \cup D$, or $B_+ \cup D_0$.*

Remark 3.1. *A simpler definition, specific to the three-dimensional case, is provided in [20, section 5]: G is Gröger-regular when Ω_0 is a bounded domain of class $W^{1,\infty}$, $\partial\Omega_{\mathrm{D}} = \partial\Omega_0 \setminus \partial\Omega_{\mathrm{N}}$ is closed, and the boundary $\partial(\partial\Omega_{\mathrm{N}})$, seen as a subset of $\partial\Omega_0$, is $W^{1,\infty}$.*

Let us mention [16, 17, 13, 20], investigating the $W^{1,q}$ or $C^{0,\alpha}$ regularity of solutions to linear and nonlinear elliptic PDEs with mixed boundary conditions. Unfortunately, these results do not apply to the linear elasticity system, for which the literature is sparser. In [46], $W^{1,q}$ regularity is obtained for solutions to the linear elastic system on a domain of class C^1. In [25], the authors extend Gröger's framework to a class of linear and nonlinear elastic systems that satisfy an ellipticity condition with respect to the linear strain tensor $\varepsilon(u)$. We state their result in the specific case of the linear elasticity system.

Proposition 3.1. *[25, Theorem 1.1] Assume that $\Omega_0 \cup \partial\Omega_{\mathrm{N}}$ is Gröger-regular, and that the Lamé coefficients μ, λ satisfy $\mu > 0$ and $2\mu + 3\lambda > 0$. Then, provided that g defines an element of $W^{-1,q}_{\mathrm{D}}(\Omega_0, \mathbb{R}^3)$, there exists a $q_0 > 2$ such that, for all $q \in [2, q_0]$, the solution to (1) is in $W^{1,q}_{\mathrm{D}}(\Omega_0, \mathbb{R}^3)$. In addition, there exists $C > 0$, depending only on Ω_0 and q, such that*

$$\|u\|_{W^{1,q}(\Omega_0)} \leqslant C \|g\|_{W^{-1,q}(\Omega_0)}.$$

Our existence result relies on the compact embedding $W^{1,q}(\Omega_0) \hookrightarrow C(\overline{\Omega}_0)$ for $q > \dim \mathbb{R}^3$ [5]. In this regard, Proposition 3.1 is not fully satisfying, as it only guarantees $q_0 > 2$. In the context of elliptic systems, the articles [26, Appendix] and [12] contain some sufficient conditions for the condition $q_0 > 3$ to hold, but it is not clear that their conditions are relevant in the case of elasticity. For this reason, we keep the condition $q_0 > 3$ as an assumption in our existence result, stated below. Note that, if we consider the same problem in $\mathbb{R}^2$, such an assumption is not necessary as $q_0 < \dim \mathbb{R}^2$ is already guaranteed by Proposition 3.1. Also, if one considers a simpler toy problem where the elastic system is replaced with an elliptic system, the existence result remains valid in any dimension without any assumption. We refer to [29, Chapter 4] for additional explanations.

Theorem 3.1. *Assume that $\Omega_0 \cup \partial\Omega_N$ is Gröger-regular and let $M > 0$.*

1. *Let us consider the equivalent of Problem (3) in $\mathbb{R}^2$. Then, Problem (3) has at least one solution.*
2. *In $\mathbb{R}^3$, assume that Ω_0 and $\partial\Omega_N$ are such that $q_0 > 3$ with the notations of Proposition 3.1. Then Problem (3) has a solution.*

3.2 Characterization of optimizers

We now turn to first-order conditions satisfied by local minimizers of Problem (3).

Before we state the optimality conditions themselves, let us have a look at the properties of the discrepancy functional J, defined in (2). In the following proposition, we state the differentiability of J. This result is fully based on Danskin's theorem [10, Chapter 3] concerning the differentiability of functions defined by a minimum. For a given displacement field $u \in C(\overline{\Omega}_0)$, we use the notation

$$P_y(u) = \{x \in S_0 \mid \|x + u(x) - y\| = d(y, S_u)\} = (\mathrm{Id} + u)^{-1} \Pi_{S_u}(y), \tag{4}$$

where $\Pi_{S_u}(y)$ is the set of orthogonal projections of y onto S_u. In particular, $P_y(u) \subset S_0$.

Proposition 3.2. *Assume that Ω_0 is bounded with Lipschitz boundary, and let $u \in C(\overline{\Omega}_0)$. Then the functional J has directional derivatives at u. Its derivative in the direction $v \in C(\overline{\Omega}_0)$ reads*

$$\mathrm{d}J(u)(v) = \int_\Gamma \min_{x \in P_y(u)} [v(x) \cdot (x + u(x) - y)] \, \mathrm{d}y. \tag{5}$$

In addition, if $P_y(u)$ is a singleton for almost every point $y \in \Gamma$, then $\mathrm{d}J(u)$ is a continuous linear form on $C(\overline{\Omega}_0)$, i.e. J is differentiable in the sense of Gateaux at u.

Though it is not Gateaux-differentiable a priori, the application J always has directional derivatives. Nondifferentiability (in the sense of Gateaux) occurs when $P_y(u)$ contains several elements for too many points in Γ. There are two reasons why $P_y(u)$ can contain several elements: either y has several orthogonal projections onto S_u, or y has a single projection point $p_{S_u}(y)$ which is the image of several points $x_1, x_2, \dots \in S_0$ under the transformation $\mathrm{Id} + u$.

Note that the directional derivative of J also reads

$$\forall v \in C(\overline{\Omega}_0), \quad \mathrm{d}J(u)(v) = \min_{\ell \in L(u)} \langle \ell, v \rangle,$$

where the set of linear forms $L(u)$ is defined by

$$L(u) = \left\{ \ell : C(\overline{\Omega}_0) \ni v \mapsto \int_\Gamma v(x_y) \cdot (x_y + u(x_y) - y) \, \mathrm{d}y \;\middle|\; x_y \in P_y(u) \right\}.$$

All the linear forms ℓ involved in the definition of $L(u)$ belong to the concave subdifferential of J, as they satisfy $\mathrm{d}J(u)(v) \leqslant \ell(v)$ for all $v \in C(\overline{\Omega}_0)$. In addition, according to the expression above, for a given direction v, there exists a family $(x_{0,y})$, with $x_{0,y} \in P_y(u)$ for all $y \in \Gamma$, such that

$$\mathrm{d}J(u)(v) = \int_\Gamma v(x_{0,y}) \cdot (x_{0,y} + u(x_{0,y}) - y)\,\mathrm{d}y.$$

We now state necessary first-order conditions that characterize a minimizer g of Problem (3). Due to the structure of the derivative $\mathrm{d}J$, the first-order conditions consist of an equality satisfied by each element $\ell \in L(u_g)$. In particular, the linear form $\ell \in L(u_g)$ associated to the family $(x_y)_{y\in\Gamma}$ is represented in the space of controls by an adjoint state p_ℓ. From a formal point of view, we aim to introduce p_ℓ as the solution to the adjoint problem

$$\left\{\begin{array}{rll} \mathrm{div}(A\varepsilon(p)) & = 0 & \text{in } \Omega_0 \\ p & = 0 & \text{on } \partial\Omega_\mathrm{D} \\ A\varepsilon(p)\cdot n & = \int_\Gamma (x_y + u(x_y) - y)\,\delta_{x_y}\,\mathrm{d}y & \text{on } \partial\Omega_\mathrm{N}, \end{array}\right. \tag{6}$$

where δ_{x_y} is the two-dimensional (pointwise) Dirac measure at x_y on $\partial\Omega_\mathrm{N}$. To rigorously define a notion of solution for such a system, we use the so-called transposition method. To this aim, we assume, as in Theorem 3.1, that Ω_0 and $\partial\Omega_N$ are such that $q_0 > 3$ with the notations of Proposition 3.1, and we consider a fixed $q \in (3, q_0]$.

For a given $h \in L^q(\partial\Omega_\mathrm{N})$, we denote by w_h the solution to the PDE

$$\left\{\begin{array}{rll} \mathrm{div}(A\varepsilon(w)) & = 0 & \text{in } \Omega_0 \\ w & = 0 & \text{on } \partial\Omega_\mathrm{D} \\ A\varepsilon(w)\cdot n & = h & \text{on } \partial\Omega_\mathrm{N}. \end{array}\right. \tag{7}$$

In what follows, q' denotes the conjugate exponent to q.

Definition 3.2. *One says that $p_\ell \in L^{q'}(\partial\Omega_\mathrm{N})$ solves (6) in the sense of transposition if*

$$\int_{\partial\Omega_\mathrm{N}} p_\ell \cdot h\,\mathrm{d}s = \int_\Gamma w_h(x_y)\cdot(x_y + u(x_y) - y)\,\mathrm{d}y.$$

for all $h \in L^q(\partial\Omega_\mathrm{N})$, where w_h solves (7).

We refer to the monography [44] for additional explanations about solutions to PDEs with measure right-hand sides, as well as the seminal work [27]. Note that, with this definition, the adjoint state p_ℓ is only defined on $\partial\Omega_\mathrm{N}$. Though the values of the adjoint state inside Ω_0 are not needed for our analysis, p_ℓ can easily be extended to the whole domain Ω_0 using (6).

Lemma 3.1. *Let us assume that $\Omega_0 \cup \partial\Omega_\mathrm{N}$ is Gröger-regular and let $q \in (3, q_0]$. Then, the adjoint problem (6) has a unique solution in the sense of transposition.*

The first-order optimality conditions are stated below.

Theorem 3.2. *Assume that $\Omega_0 \cup \partial\Omega_\mathrm{N}$ is Gröger-regular and $M \in [0, \infty]$. Let $g \in \mathcal{G}_M$ a local minimizer of Problem (3) and u_g the associated displacement field. If $\ell \in L(u)$, denote by p_ℓ the associated adjoint state defined by (6). For every $\ell \in L(u)$, there exists a Lagrange multiplier $\lambda_\ell \in L^2(\partial\Omega_\mathrm{N}, \mathbb{R})$, with*

$$\text{for a.e. } x \in \partial\Omega_\mathrm{N} \quad \left\{\begin{array}{ll} \lambda_\ell(x) = 0 & \text{if } \|g(x)\| < M \\ \lambda_\ell(x) \geqslant 0 & \text{if } \|g(x)\| = M, \end{array}\right.$$

such that g satisfies the first-order optimality condition

$$\text{for a.e. } x \in \partial\Omega_\mathrm{N} \qquad p_\ell(x) + \lambda_\ell(x) g(x) = 0.$$

Remark 3.2 (Practical use of optimality conditions.)**.** *It is notable that if $g \in \mathcal{G}_M$ is a local minimizer of Problem (3) such that $\|g\| < M$ almost everywhere on $\partial\Omega_{\mathrm{N}}$, then Φ is Gateaux-differentiable at g with $\mathrm{d}\Phi(g)(\cdot) = 0$. Indeed, if the L^∞ constraint is inactive, then $\lambda_\ell = 0$ by the so-called slackness property. In this case, the optimality condition simply reads $p_\ell = 0$ on $\partial\Omega_N$. Using (6), we obtain $\ell = 0$, and therefore $L(u_g) = \{v \mapsto 0\}$, which means that Φ is Gateaux-differentiable at g.*

This comment is relevant for the numerical implementation. In practice, even though we take into account the L^∞ constraint in the numerical algorithm, we observe that this constraint is not saturated as soon as M is chosen large enough. This suggests (but this is only a numerical conjecture) that the problem still has a solution if we remove the L^∞ constraint in the optimal control problem definition.

Furthermore, it can be easily checked that it is only necessary to find one projection per point $y \in \Gamma$ when evaluating J. Indeed, according to Proposition 3.2, if $\ell_0 \in L(u)$ is given and if v is chosen so that $\langle \ell_0, v\rangle \leq 0$, then,

$$\mathrm{d}J(u)(v) = \min_{\ell \in L(u)} \langle \ell, v\rangle \leqslant \langle \ell_0, v\rangle \leqslant 0,$$

meaning that v is also a descent direction for the whole criterion J.

3.3 Numerical solving

To solve the registration problem numerically, we discretize the optimal control formulation using P1 finite element functions. Due to the complex geometry of organs, using a tetrahedron mesh is very common in augmented surgery. In addition, choosing piecewise linear functions is more convenient when it comes to computing orthogonal projections onto the deformed mesh.

We adopt a 'discretize-then-optimize' approach, which means that the entire formulation is transformed into a finite-dimensional problem, which is then solved using numerical tools for finite-dimensional optimization. Indeed, an algorithm based on the 'optimize-then-discretize' might be very sensitive to discretization errors, and might encounter difficulties to find adequate directions of descent by applying the continuous approach on a discretized problem. We have therefore chosen to adapt *mutatis mutandis* the tools developed in the previous section to a discrete framework.

From now on, the discrete displacement field is represented by the finite-dimensional vector $\mathbf{u} = (u_1, \dots, u_n) \in \mathbb{R}^{3n}$ where n is the number of vertices and $u_k \in \mathbb{R}^3$ is the displacement of the k-th vertex. The same bold letter $\mathbf{u}$ is used to denote the associated finite element function. We control the vector of nodal forces $\mathbf{b} = (b_1, \dots, b_n)$ at the mesh vertices, and a displacement is determined by solving the linear system

$$\mathbf{A}\mathbf{u} = \mathbf{b},$$

where $\mathbf{A}$ is the stiffness matrix. Note that controlling directly the nodal forces $\mathbf{b}$ instead of the surface force distribution is a good way to lighten computations, at the expense of consistency with the continuous problem. It remains consistent with the discretize-then-optimize approach, though.

Discrete objective function. Let us first have a look at the discretized functional J. In the discretized framework, the organ surface $\partial\Omega_0$ is a triangular mesh, and defining S_0 consists in selecting the set of triangles that is used to evaluate J. The observation Γ is provided as the point cloud $\Gamma = \{y_1, \dots, y_p\} \subset \mathbb{R}^3$, and the discretized functional reads

$$J(\mathbf{u}) = \tfrac{1}{p}\sum_{i=1}^{p} j_i(\mathbf{u}) \quad \text{where} \quad j_i(\mathbf{u}) = \tfrac{1}{2} d^2(y_i, S_{\mathbf{u}}). \tag{8}$$

Our implementation uses the nearest-neighbour search from the Trimesh Python package[1] to evaluate the distance between a point $y \in \Gamma$ and $S_{\mathbf{u}}$. This projection procedure stores triangles from $S_{\mathbf{u}}$ in a

[1] Website: https://trimsh.org

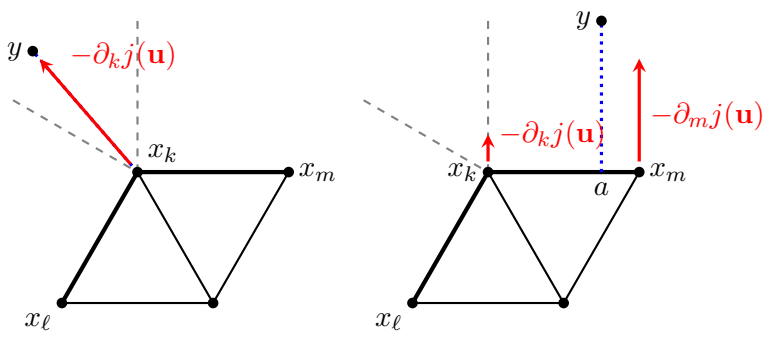

Figure 2: Illustration of $\nabla j(\mathbf{u})$ in two configurations. Points x_ℓ, x_k and x_m are located on the mesh boundary, while the last vertex is inside the mesh. The red arrows represent the components of the descent direction $-\nabla j(\mathbf{u})$. On the right, the equality $y - a = -\partial_k j(\mathbf{u}) - \partial_m j(\mathbf{u})$ holds.

spatial indexing structure [19] to perform efficient nearest-neighbour queries. Using Remark 3.2 and the fact that nondifferentiability only occurs on a negligible subset of the space of displacements, we only need the nearest-neighbour search procedure to return a single projection point $a = p_{S_\mathbf{u}}(y)$ per observed point $y \in \Gamma$. Note that handling an unknown number of projections per point y would represent an additional computational cost, and would require special attention to avoid computing every p_ℓ. We have therefore chosen a compromise between efficiency and complexity of the algorithm.

Since we are dealing with piecewise linear finite element functions, differentiating J with respect to the displacement field $\mathbf{u}$ means differentiating J with respect to the displacements $(u_1, \cdots, u_n)$ at the mesh vertices. Thus, the gradient $\nabla J(\mathbf{u})$ is defined by its vertex-wise components $(\partial_1 J(\mathbf{u}), \cdots, \partial_n J(\mathbf{u}))$. We first consider the elementary application $j(\mathbf{u})$, where we have dropped the index i compared to (8). Given a displacement field $\mathbf{u}$, we denote by $\mathbf{x}^0$ and $\mathbf{x}$ the initial and current positions of the mesh vertices, respectively. In particular, $\mathbf{x}^0$ and $\mathbf{x}$ satisfy $\mathbf{x}^0 + \mathbf{u} = \mathbf{x}$.

Assume that the projection point $a = p_{S_\mathbf{u}}(y)$ falls into the triangle composed of vertices k_1, k_2, k_3. We use the notations

$$a = \theta_1 x_{k_1} + \theta_2 x_{k_2} + \theta_3 x_{k_3} \quad \text{and} \quad a^0 = \theta_1 x^0_{k_1} + \theta_2 x^0_{k_2} + \theta_3 x^0_{k_3},$$

where the (nonnegative) barycentric coefficients θ_1, θ_2, θ_3 satisfy $\theta_1 + \theta_2 + \theta_3 = 1$. In particular, $a = a^0 + \mathbf{u}(a^0)$. For $\mathbf{v}$ a perturbation of $\mathbf{u}$, we obtain after adapting (5)

$$\langle \mathrm{d}j(\mathbf{u}), \mathbf{v} \rangle = \mathbf{v}(a^0) \cdot (a - y) = (\theta_1 v_{k_1} + \theta_2 v_{k_2} + \theta_3 v_{k_3}) \cdot (a - y)\,.$$

Therefore, the gradient $\nabla j(\mathbf{u})$ satisfies

$$\forall i \in \{1,2,3\} \quad \partial_{k_i} j(\mathbf{u}) = \theta_i (a - y) \qquad \forall k \notin \{k_1, k_2, k_3\} \quad \partial_k j(\mathbf{u}) = 0.$$

Finally, the gradient $\nabla J(\mathbf{u})$ reads

$$\nabla J(\mathbf{u}) = \tfrac{1}{p} \sum_{i=1}^{p} \nabla j_i(\mathbf{u}).$$

Figure 2 illustrates the components of $\nabla j(\mathbf{u})$ in a two-dimensional configuration.

Adjoint method. As suggested by the problem formulation in (3), we solve the optimization problem numerically using an adjoint method, where the only variable controlled by the optimization solver is the nodal force distribution $\mathbf{b}$. Keeping the same notations as in (3), the discrete optimization problem reads

$$\min_{\mathbf{b} \in \mathcal{B}} \quad \Phi(\mathbf{b}) \quad \text{where} \quad \Phi(\mathbf{b}) = J(\mathbf{u}_\mathbf{b}). \tag{9}$$

Here, the elasticity system is hidden in the objective function Φ and has to be interpreted as an equality constraint of the optimization problem. In particular, each evaluation of the objective value $\Phi(\mathbf{u})$ requires to solve the elasticity system to compute $\mathbf{u_b}$.

Now, to solve (9) using a first-order optimization method, computing the objective gradient $\nabla\Phi(\mathbf{b})$ is also required. The adjoint method exploits the first-order optimality conditions derived in Remark 3.2, keeping in mind that we only consider the differentiable case here. In a similar fashion to (6), we define the adjoint state $\mathbf{p_b}$, solution to the adjoint elasticity system

$$\mathbf{A}\mathbf{p} = \nabla J(\mathbf{u_b}).$$

An immediate adaptation of the proof of Theorem 3.2 yields

$$\nabla\Phi(\mathbf{b}) = \mathbf{p_b}.$$

Algorithm 1 shows the outline of the adjoint procedure.

Adjoint methods are convenient as they result in modular implementations, where each part may be taken care of by a separate entity. In particular, it is easy to switch functionals, mechanical models or optimization solvers, as they only communicate through simple interfaces. Our implementation [2] relies on the Numpy framework. The stiffness matrix is assembled using the SOFA finite element software developed by the Inria Mimesis Team [2], then it is factorized before the procedure starts. Concerning the optimization procedure itself, it is taken care of by off-the-shelf solvers available in the Scipy library, namely a limited-memory quasi-Newton solver [6].

Algorithm 1: Computation of the objective gradient using an adjoint method.

Data: Current iterate $\mathbf{b}$
Compute the displacement $\mathbf{u_b}$ by solving $\mathbf{A}\mathbf{u} = \mathbf{b}$
Evaluate $J(\mathbf{u_b})$ and $\nabla J(\mathbf{u_b})$
Compute the adjoint state $\mathbf{p_b}$ by solving $\mathbf{A}\mathbf{p} = \nabla J(\mathbf{u_b})$
Result: $\nabla\Phi(\mathbf{b}) = \mathbf{p_b}$

4 Numerical results

We now present a few numerical examples involving the adjoint method. First, we illustrate the convergence properties of the optimization procedure on a toy problem. It is also the occasion to clarify what can or can't be expected from the method in terms of registration accuracy. Then we show an example in a registration scenario involving the Sparse Data Challenge dataset. In our last result, we opt for a neo-Hookean elastic model and take profit of a simple registration scenario to illustrate the feasibility of choosing a nonlinear model.

4.1 A toy problem

Let us begin with an unpleasant remark: though registration error might be reduced by taking physical considerations into account, our registration method comes with no guarantee in terms of displacement accuracy. To illustrate this disclaimer, we evaluate the displacement error of the procedure on a toy problem.

We create a truncated sphere mesh with radius 1, where the distance from the sphere centre to the truncating plane is $1/2$. The mesh contains 10,385 nodes and 6,702 triangular faces. The flat surface of the mesh is subject to a Dirichlet condition, while forces are applied on the round surface to generate

[2] Our code is available at the following url: https://github.com/gmestdagh/adjoint-elastic-registration.

a displacement. A linear elastic model is used, with $E = 1$ and $\nu = 0.49$. After the elastic deformation is applied to the mesh, the round surface is sampled to create a point cloud of 10,000 points. Figure 3a shows the initial mesh and the synthetic deformation.

We create very favourable conditions for the registration procedure. First, the point cloud, very dense and noise-free, provides a good representation of the deformed surface. In addition, the same mesh is used for data creation and for reconstruction, which evacuates possible discrepancies between two meshes representing the same shape. Figure 3b shows the objective value and gradient norm along iterations of the optimization solver. After 176 iterations, the gradient norm has decreased by 5 orders of magnitude. The objective function keeps decreasing and evaluates to $2 \cdot 10^{-7}$ as the procedure ends, meaning that the quadratic mean of the distance between data points and the deformed surface is approximately $6 \cdot 10^{-4}$. Figure 4a shows the point cloud, along with a superposition of the true (green) and reconstructed (yellow) surfaces, confirming the good matching between surfaces.

Despite a tight surface matching, the displacement error (Figure 3c) settles around 10^{-1}, with a maximum error of 0.6 (the sphere radius is 1). In Figure 4b, we illustrated the displacement discrepancy between the true (green) and reconstructed (yellow) surfaces. The displacement error is plotted in Figure 4c. Without surprise, the displacement error increases as we move away from the Dirichlet boundary condition. The last graph in Figure 3c shows the error on nodal forces for the 2,522 vertices of the Neumann surface. The nodal force errors settle to the same order of magnitude as the nodal forces themselves, suggesting an average 100% error. In general, it should be difficult to give a meaning to the reconstructed distribution, especially when it contains many degrees of freedom.

Should we give up every hope for all that? Actually, the sphere test case is not as easy as it seems. Due to the sphere's symmetry, the registration method has no clue about the best way to match the point cloud. As a consequence, generating an inaccurate displacement is costless, as long as the deformed surface matches the point cloud. In the case of an organ, things are different, as the point cloud reflects the shape of the surface part it is supposed to match. In addition, in the application case, some landmarks, detected by the laparoscopic camera [43, Figure 3], may be used to improve registration accuracy.

4.2 Sparse Data Challenge dataset

In this section, we present an organ registration result in the context of augmented surgery. This example, developed in our conference paper [30, Section 3.1], involves the *Sparse Data Challenge*[3] dataset. The dataset contains one tetrahedral mesh representing a silicon liver phantom in its initial configuration and 112 point clouds acquired from 112 deformed configurations of the same phantom [8, 4]. To generate deformations, the challenge organizers laid the phantom on irregular supports on its posterior face [45, Figure 2]. They produced the point clouds by acquiring pictures of the anterior face with a camera. The phantom also contains 159 targets whose position is measured in reference and deformed configurations to establish ground truth data. The position of targets remains unknown to us, and the registration error is computed by the challenge website after we upload a reconstructed mesh position associated with each point cloud. By keeping the ground truth hidden from participants, the challenge organizers eliminate bias associated with knowledge of the ground truth.

To begin with, we perform a rigid alignment between the initial mesh and the point cloud using the Iterative closest point algorithm [3], and afterwards we set a homogeneous Dirichlet boundary condition on a small zone in the liver posterior face to enforce existence and uniqueness of a solutions to the elasticity system. The Dirichlet boundary is chosen arbitrarily, as available information does not suggest an area rather than another. Here, the deformation is caused by the irregular support applying contact forces on the posterior surface, and for this reason we label the posterior surface as the *loaded surface*, where nodal forces are allowed to take nonzero values. On the other hand, the point cloud represents the anterior surface, and in this case, the anterior surface is selected as the *matching surface*

[3]Challenge website: sparsedatachallenge.org.

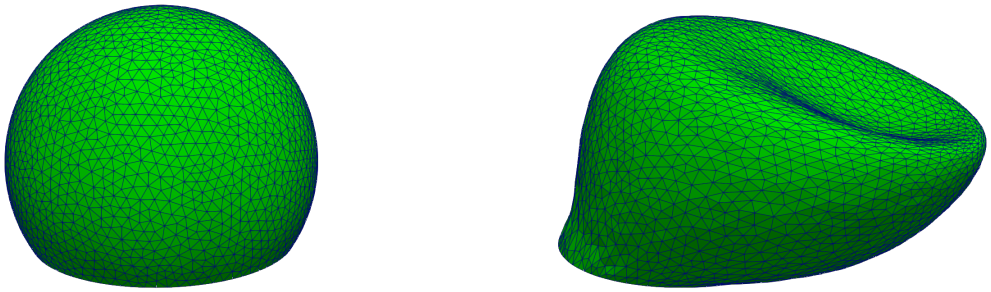

(a) Initial sphere mesh (left) and synthetic deformation (right).

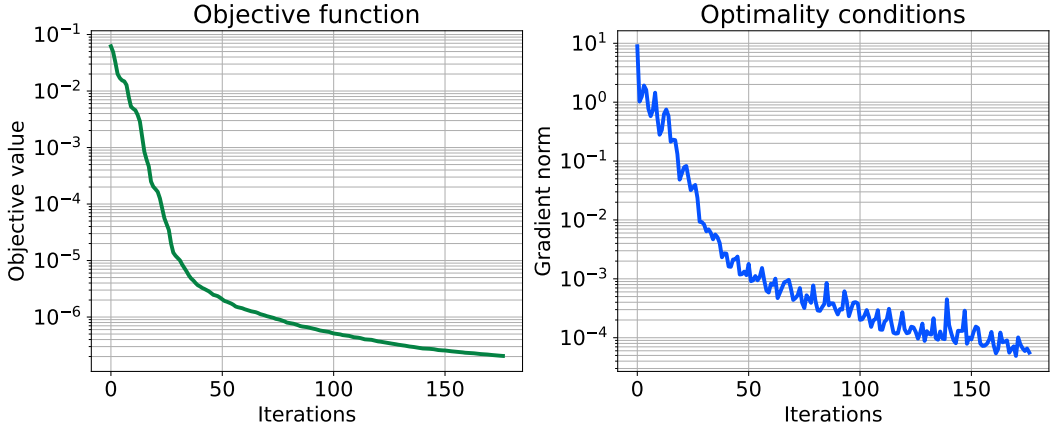

(b) Objective value and gradient norm along iterations.

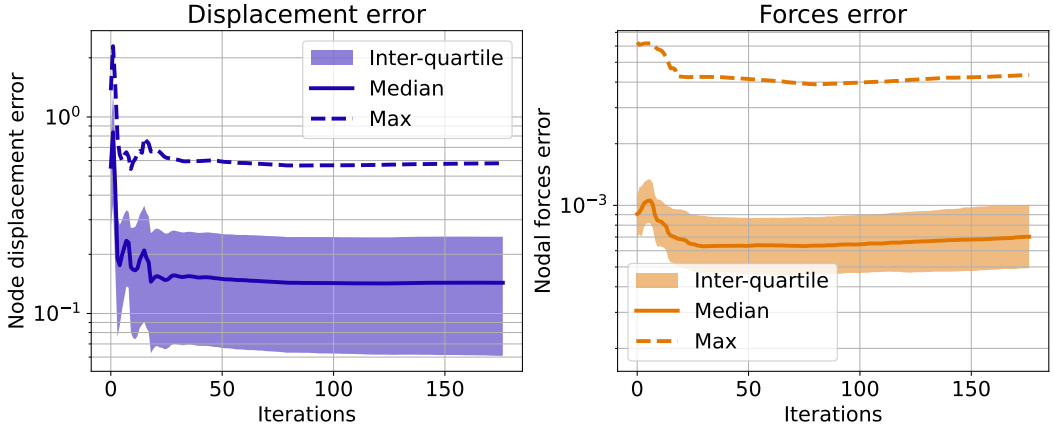

(c) Reconstruction error statistics for vertex displacements and nodal forces.

Figure 3: Synthetic deformation and convergence statistics for the toy problem.

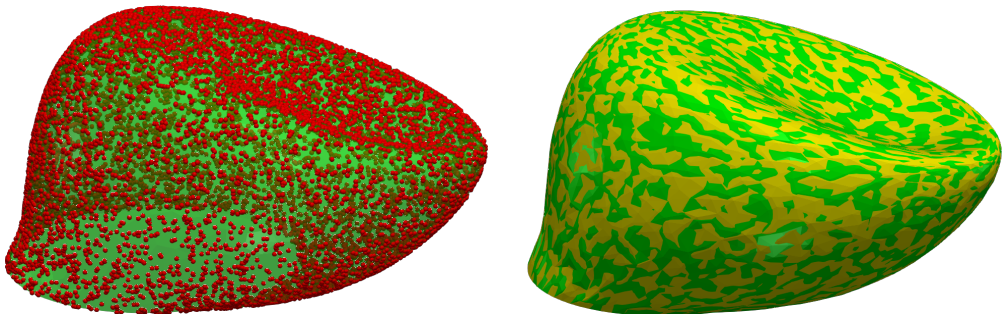

(a) Point cloud and superposition of the true and reconstructed surface.

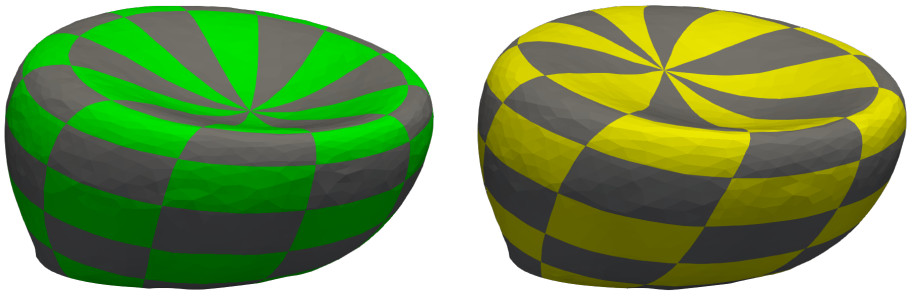

(b) Discrepancy between the true (left) and reconstructed (right) surface.

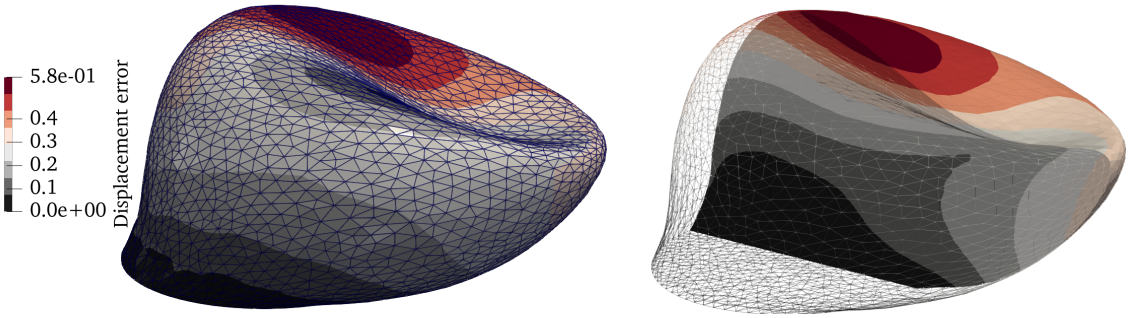

(c) Displacement error.

Figure 4: Registration results for the toy problem.

S_0. Figure 5a shows the initial mesh with the two labelled surfaces. We run the adjoint method, using a linear elastic model with $E = 1$ and $\nu = 0.4$, and we stop the procedure after 200 iterations. The resulting deformations in four cases are shown in Figure 5b.

Displacement errors for the whole dataset are gathered in Table 5c. In Figure 5d, they are compared with other submissions displayed on the challenge website. We obtain the second-best result among submissions that appear on the challenge website. Despite a greater sensibility to surface coverage than the leading team, our average registration error remains well below the 5 mm limit required by our clinical partners. This results highlight the interest of methods based on an inverse problem in intra-operative organ registration.

4.3 Toward nonlinear mechanics

All theoretical and numerical results presented until now rely on the linear elastic model. However, while linear elasticity is only relevant for small deformations, organs are made of soft living tissues undergoing large deformations, and a successful registration procedure should allow hyperelastic deformations. In this section, we illustrate the extension of our results to nonlinear elasticity on a simple example.

We consider a liver mesh with 3,046 vertices, embedded with a Neo-Hookean model. Dirichlet boundary conditions are applied at the hepatic vein entry and in the falciform region. We create a synthetic deformation by applying a local force on one lobe of the liver, and we sample the deformed surface to create a point cloud with 500 points. We perform the registration using the same mesh and elastic model. The reconstructed force distributions is restricted to a zone slightly larger than the zone used to generated the deformation.

A few modifications are required in the adjoint pipeline to use hyperelastic models. In particular, the direct problem is now a nonlinear variational equation, denoted

$$\mathbf{F}(\mathbf{u}) = \mathbf{b}.$$

It is usually solved using a Newton [18, 50] or quasi-Newton [15, 51] method. In the Neo-Hookean case, though, ensuring stability of the iterative method is critical to avoid generating displacement fields where the elastic residual $\mathbf{F}(\mathbf{u})$ cannot be evaluated. For this reason, we use a trust-region Newton method, for which convergence is guaranteed. Note that the adjoint problem is the linear system

$$\mathbf{F}'(\mathbf{u_b})\mathbf{p} = \nabla J(\mathbf{u_b}),$$

where the residual Jacobian $\mathbf{F}'(\mathbf{u_b})$ is evaluated at the solution of the direct problem.

Figure 6 show registration examples involving the Neo-Hookean model. It is noteworthy that the number of iterations if the optimization solver is very different between cases. Actually, the registration procedure did not stop because the optimality tolerance was met, but because the iterative direct solver accuracy was not sufficient for the optimization solver to keep generating descent directions. In each case, the original deformation is shown side by side with the reconstructed deformation. The arrows represent nodal forces. Note that the reconstructed force distribution is much noisier and messier than the true one, but it somehow exhibits a trend in the right direction.

These results illustrate the feasibility of the optimal control approach for hyperelastic organ registration. Subsequent work should seek to produce a more mature and efficient procedure involving the nonlinear model.

5 Discussion and Conclusion

The first numerical results from the implementation of the method described in this paper are very encouraging, even when considering nonlinear elasticity models. We conclude by mentioning below some avenues of improvement that are the subject of current and future work.

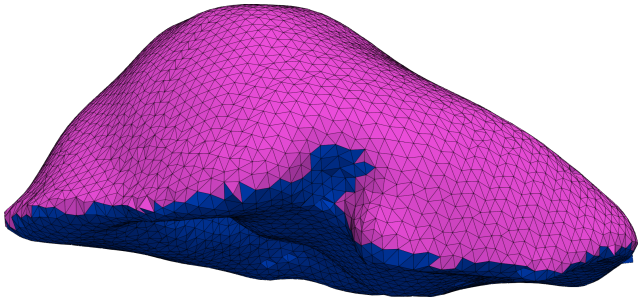

(a) Initial mesh. The bottom surface (in blue) is the loaded surface while the top surface (in magenta) is the matching surface.

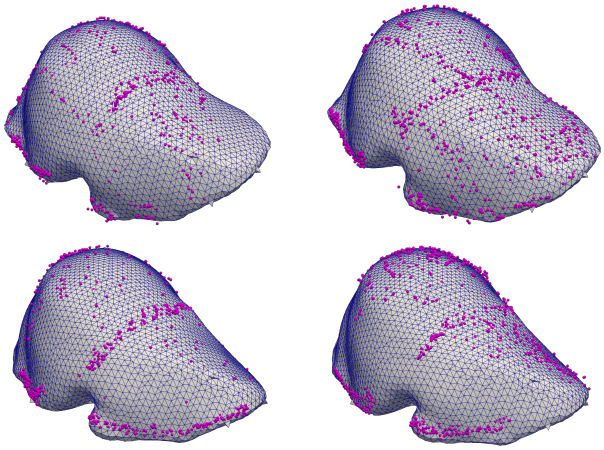

(b) Point cloud (magenta) and reconstructed deformations for four cases.

Surface Coverage	Average	Standard deviation	Median
20-28 %	3.54	1.11	3.47
28-36 %	3.27	0.85	3.19
36-44 %	3.13	0.82	3.13
All data sets	3.31	0.94	3.19

(c) Target registration error statistics (in millimeters) for all datasets, as returned by the website after submission.

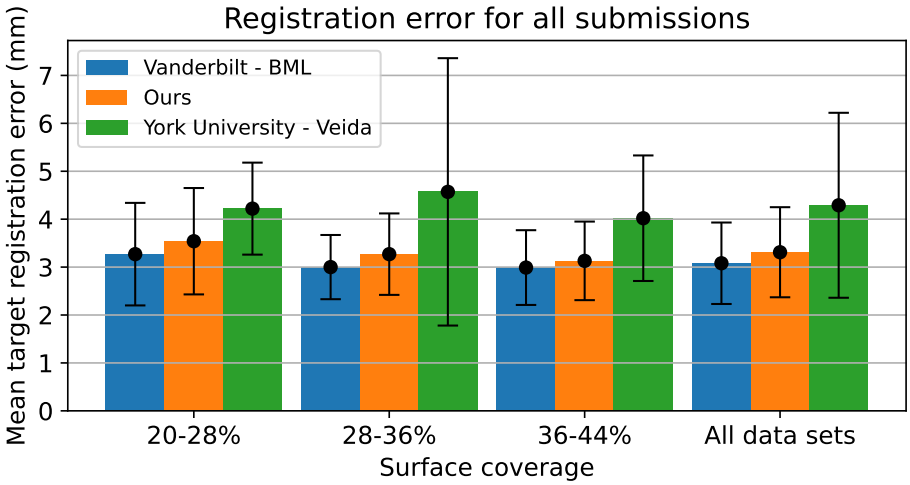

(d) Comparison of our TRE results with other participants (our column is the middle one).

Figure 5: Results for the *Sparse Data Challenge* dataset [30].

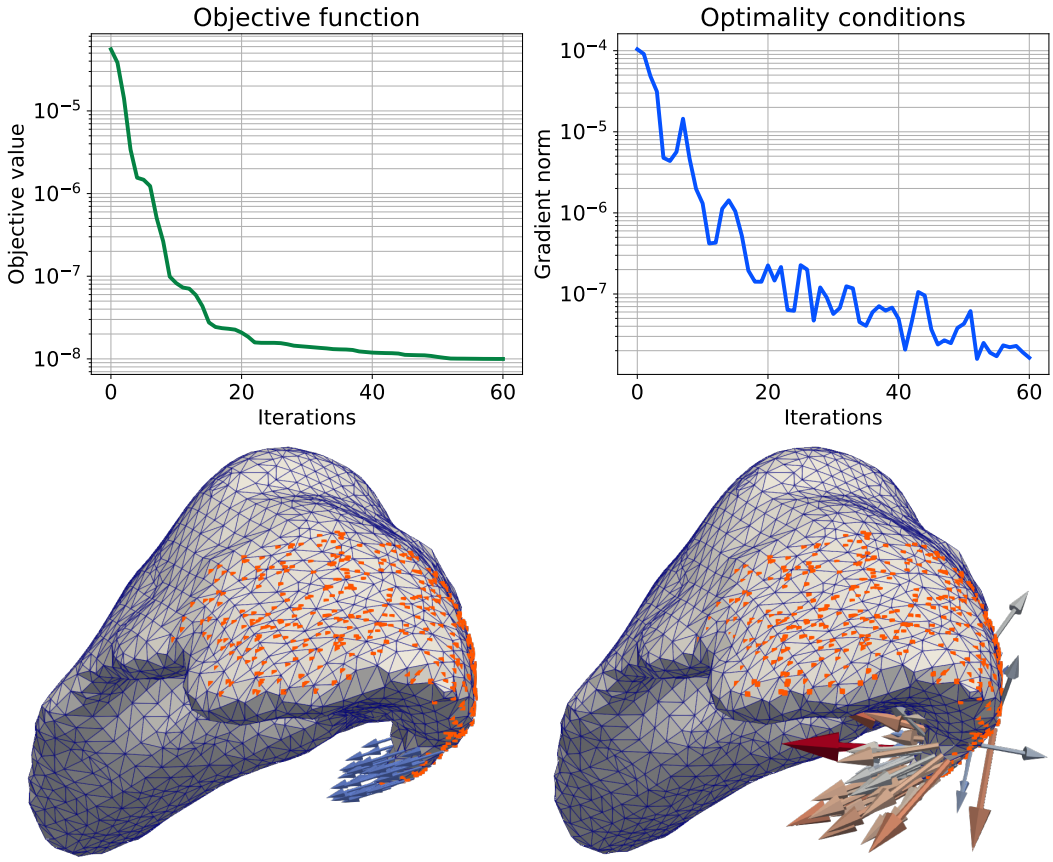

(a) Case 1.

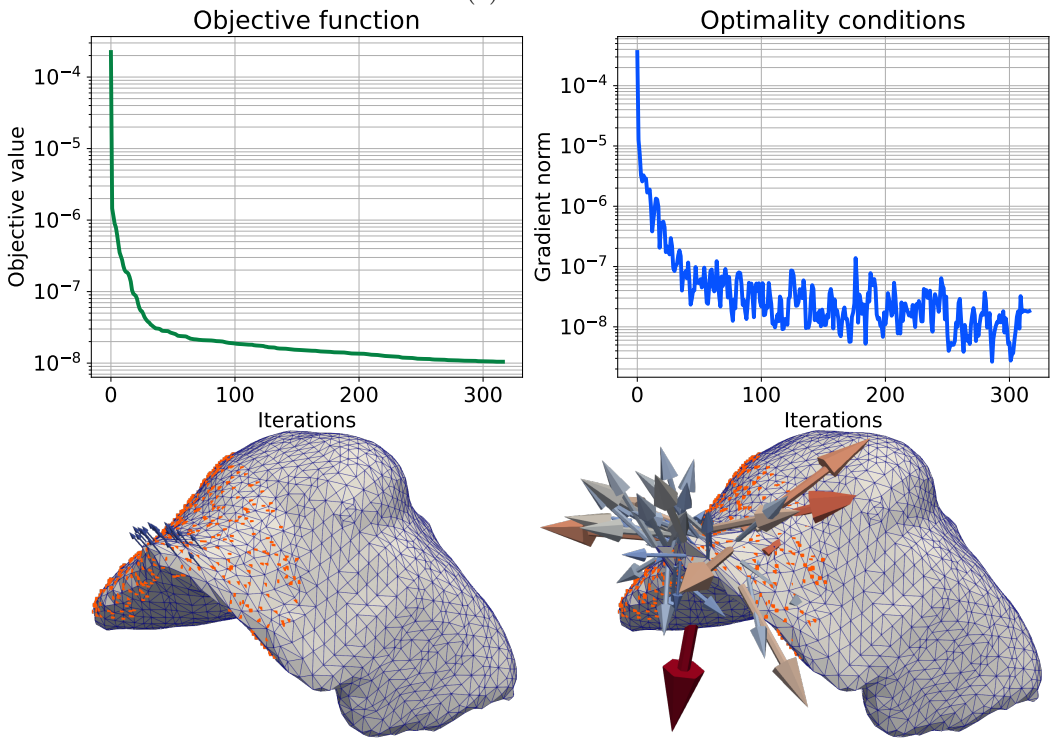

(b) Case 2.

Figure 6: Convergence statistics (top), along with the true and reconstructed deformations (bottom) for two test cases with the nonlinear model.

Let us first comment the choice to consider static elasticity problems involving a Dirichlet boundary condition. The main role of the Dirichlet boundary condition here is to guarantee the well-posed character of the direct and optimal control problems, in particular the existence and uniqueness of a solution displacement u given a force distribution g. Its role is also, to a lesser extent, to take into account anatomical factors that limit the organ motion. In liver surgery, the Dirichlet condition is often set at the hepatic vein entry, or sometimes at places where ligaments hold the liver (e.g. the falciform region). However, we believe that the whole procedure could benefit from a finer modelling of those movement restrictions. We plan to no longer consider a Dirichlet hard-constraint, but instead account for the presence of the hepatic vein entry using penalty terms in the cost functional.

On another level, even though we made choices in order to make the algorithm as light as possible, the question of computation time still needs to be addressed. The adjoint method shares processor time with other parts of the pipeline, including point cloud generation from laparoscopic images and displaying the augmented view. In this article, we do not clarify whether achieving real-time registration using the adjoint method is feasible, even with a better implementation of the adjoint procedure and a good trade-off between accuracy and computation cost. For this reason, we are developing an implementation where the iterative nonlinear elastic solver is replaced with an artificial neural network. Preliminary results [37] show a significant speed-up of the procedure due to the efficiency of neural networks.

Finally, we are currently thinking about modeling issues, around the choice of cost functionals, in order to improve the robustness against possible measurement errors on the Γ points. Indeed, we have in practice a cloud of points allowing to reconstruct Γ. We would like to introduce a *worst-case* functional to make the result as insensitive as possible to possible measurement errors on the data.

A Proofs of Proposition 3.2, Theorem 3.1 and Theorem 3.2

In this section we provide details about the results stated in Section 3.

A.1 Proof of Proposition 3.2

The continuous version of J reads

$$J(u) = \int_\Gamma j_y(u)\,\mathrm{d}y \quad \text{where} \quad j_y(u) = \tfrac{1}{2}d^2(y, S_u).$$

We begin by studying the properties of the elementary functional j_y in a first lemma, and then we finish the proof of Proposition 3.2 using the dominated convergence theorem. Remember that the definition of $P_y(u)$ is given in (4).

Lemma A.1. *Let y a fixed point in Γ. The application j_y is locally Lipschitz continuous on $C(\overline{\Omega}_0)$. The Lipschitz constant can be chosen independent from y but still depends on Γ. In addition, for $u \in C(\overline{\Omega}_0)$, j_y has directional derivatives. The directional derivative in the direction $v \in C(\overline{\Omega}_0)$ reads*

$$\mathrm{d}j_y(u)(v) = \min_{x \in P_y(u)} v(x) \cdot (x + u(x) - y).$$

Proof. Recalling that $S_u = (\mathrm{Id} + u)(S_0)$, we write $j_y(u) = \min_{x \in S_0} \frac{1}{2}\|x + u(x) - y\|^2$.

First, we check Lipschitz continuity. Let $u_1, u_2 \in C(\overline{\Omega}_0)$. As S_0 is compact, there is a $x_1 \in S_0$ with $j_y(u_1) = \frac{1}{2}\|x_1 - u_1(x_1) - y\|^2$. Then,

$$\begin{aligned} j_y(u_2) - j_y(u_1) &\leqslant \tfrac{1}{2}\|x_1 + u_2(x_1) - y\|^2 - \tfrac{1}{2}\|x_1 + u_1(x_1) - y\|^2 \\ &= \tfrac{1}{2}(2x_1 + u_2(x_1) + u_1(x_1) - 2y) \cdot (u_2(x_1) - u_1(x_1)) \\ &\leqslant \left(\max_{x \in S_0} \|x - y\| + \tfrac{1}{2}\|u_2 + u_1\|_{L^\infty(\Omega_0)}\right) \|u_2 - u_1\|_{L^\infty(\Omega_0)}, \end{aligned}$$

As Γ is compact, we obtain the Lipschitz constant

$$L = \max_{y\in\Gamma}\left(\max_{x\in S_0}\|x-y\|\right) + \tfrac{1}{2}\|u_2+u_1\|_{L^\infty(\Omega_0)}.$$

To compute directional derivatives, we define the application

$$\begin{array}{rccc} f: & \mathbb{R}_+\times S_0 & \to & \mathbb{R} \\ & (t,x) & \mapsto & \frac{1}{2}\|x+u(x)+tv(x)-y\|^2, \end{array}$$

and we note that $j_y(u+tv) = \min_{x\in P_y(u+tv)} f(t,x)$. The partial derivative $\partial_t f$ exists and is continous, and for $t>0$ the set $P_y(u+tv)$ is nonempty and compact. All conditions are gathered to apply Danskin's theorem [10, Chapter 3, Theorem I], which stipulates that j_y is differentiable at u in the direction v, with

$$\mathrm{d}j_y(u)(v) = \lim_{t\searrow 0}\frac{j_y(u+tv)-j_y(u)}{t} = \min_{x\in P_y(u)}\partial_t f(0,x),$$

which is the formula we wanted to end up with. □

We now use the dominated convergence theorem to finish the proof. Denote by $B=B(0,r)$ a small ball of radius $r>0$. As j_y is Lipschitz continuous on $u+B$, there is a constant L independent from y such that

$$\forall v\in B\ \forall t\in(0,1)\quad \left|\frac{j_y(u+tv)-j_y(u)}{t}\right| \leqslant L\|v\|_{L^\infty(\Omega_0)} \leqslant Lr.$$

Using the dominated convergence theorem, we pass to the limit in the expression

$$\frac{J(u+tv)-J(u)}{t} = \int_\Gamma \frac{j_y(u+tv)-j_y(u)}{t}\,\mathrm{d}y \xrightarrow[t\searrow 0]{} \int_\Gamma \mathrm{d}j_y(u)(v)\,\mathrm{d}y$$

to obtain the derivative.

Now, if $P_y(u)$ is a singleton $\{x_y\}$ for almost every $y\in\Gamma$, we obtain

$$\langle \mathrm{d}J(u), v\rangle = \int_\Gamma v(x_y)\cdot(x_y+u(x_y)-y)\,\mathrm{d}y \leqslant |\Gamma|\left(\max_{y\in\Gamma} d(y,S_u)\right)\|v\|_{L^\infty(\Omega_0)},$$

i.e. $\mathrm{d}J(u)$ is a continuous linear form.

A.2 Proof of Theorem 3.1

Consider a minimizing sequence (g_j) of elements of $\mathcal{G}_M$. As (g_j) is bounded in $L^\infty(\partial\Omega_{\mathrm{N}})$, it converges $\star$-weakly in $L^\infty(\partial\Omega_{\mathrm{N}})$, towards a limit that we denote g. As $\mathcal{G}_M$ is closed for the weak-$\star$ topology, g is an element of $\mathcal{G}_M$. We denote respectively by $u_j = u_{g_j}$ the state associated to g_j and by $u=u_g$ the state associated to g. The proof falls into two parts. We first prove that the sequence (u_j) converges towards u, and then we finish the proof by showing that the convergence is uniform.

The state equations for u_j and u yield

$$\begin{aligned} \forall v\in H^1_{\mathrm{D}}(\Omega)\quad & \int_{\Omega_0} A\varepsilon(u_j):\varepsilon(v)\,\mathrm{d}x = \int_{\partial\Omega_{\mathrm{N}}} g_j\cdot v\,\mathrm{d}s \\ \forall v\in H^1_{\mathrm{D}}(\Omega)\quad & \int_{\Omega_0} A\varepsilon(u):\varepsilon(v)\,\mathrm{d}x = \int_{\partial\Omega_{\mathrm{N}}} g\cdot v\,\mathrm{d}s. \end{aligned}$$

Taking into account the weak-$\star$ convergence of (g_j) towards g leads to

$$\forall v\in H^1_{\mathrm{D}}(\Omega)\quad \int_{\Omega_0} A\varepsilon(u_j):\varepsilon(v)\,\mathrm{d}x \to \int_{\Omega_0} A\varepsilon(u):\varepsilon(v)\,\mathrm{d}x. \tag{10}$$

As $\partial\Omega_{\mathrm{D}}$ has positive measure in $\partial\Omega$, the linear elasticity bilinear form is an inner product on $H^1_{\mathrm{D}}(\Omega_0)$ [7, Theorems 6.3-3 and 6.3-4], and (10) is equivalent to $u_j \rightharpoonup u$ in $H^1_{\mathrm{D}}(\Omega_0)$. In particular, $u_j \rightharpoonup u$ in $L^2(\Omega_0)$.

We now check that (u_j) converges uniformly. Let q the exponent from Proposition 3.1 and denote by $q' = q/(q-1)$ its conjugate exponent. Remember that we assumed $q > 3$. Note that the trace $v|_{\partial\Omega_{\mathrm{N}}}$ of a function $v \in W^{1,q'}_{\mathrm{D}}(\Omega_0)$ is in $L^{q'}(\partial\Omega_{\mathrm{N}})$ [14, §5.5, Theorem 1]. This confirms that an element of $L^\infty(\partial\Omega_{\mathrm{N}}) \subset L^{q'}(\partial\Omega_{\mathrm{N}})'$ represents an element of $W^{-1,q}_{\mathrm{D}}(\Omega_0)$ (with continuous injection). Because elements of (g_j) are in $\mathcal{G}_M$, the sequence is bounded in $W^{-1,q}_{\mathrm{D}}(\Omega_0)$. Then, due to Proposition 3.1, the sequence (u_j) is uniformly bounded in $W^{1,q}_{\mathrm{D}}(\Omega_0)$, and, as a consequence of the Rellich-Kondrachov theorem [1, Theorem 6.3], it converges uniformly, up to a subsequence. We check that the uniform limit is u by noting that uniform convergence implies weak convergence in L^2.

Finally, as J is continuous on $C(\overline{\Omega}_0)$, we obtain that $J(u) = \lim J(u_j) = \min_{\mathcal{G}_M} \Phi$, and g is a solution to (3).

A.3 Proof of Lemma 3.1

Let us construct the solution with the help of an approximation process. We first consider a single point $y \in \Gamma$, and we denote $z = x_y + u(x_y) - y \in \mathbb{R}^3$. We look for an elementary adjoint state $p_{\ell,y}$ such that

$$\forall h \in L^q(\partial\Omega_{\mathrm{N}}) \quad \int_{\partial\Omega_{\mathrm{N}}} p_{\ell,y} \cdot h \,\mathrm{d}s = w_h(x_y) \cdot z. \tag{11}$$

The regularity assumption on $\partial\Omega_{\mathrm{N}}$ yields to the existence of a family of bounded open subsets ω_δ of $\partial\Omega_{\mathrm{N}}$, and such that $(\omega_\delta)_{\delta>0}$ shrinks to $\{x_y\}$ as $\delta \searrow 0$. Setting $f_\delta = \mathbf{1}_{\omega_\delta}/\mathcal{H}^2(\omega_\delta)$, where $\mathcal{H}^2(\omega_\delta)$ is the two-dimensional Hausdorff measure of ω_δ, we introduce p_δ as the solution of the PDE

$$\left\{\begin{array}{rll} \mathrm{div}(A\varepsilon(p_\delta)) & = 0 & \text{in } \Omega_0 \\ p_\delta & = 0 & \text{on } \partial\Omega_{\mathrm{D}} \\ A\varepsilon(p_\delta)\cdot n & = f_\delta\, z & \text{on } \partial\Omega_{\mathrm{N}}, \end{array}\right.$$

According to Proposition 3.1, one has $p_\delta \in W^{1,q}_{\mathrm{D}}(\Omega_0)$, and using the Green formula, one gets

$$\forall h \in L^q(\partial\Omega_{\mathrm{N}}) \quad \int_{\partial\Omega_{\mathrm{N}}} p_\delta \cdot h \,\mathrm{d}s = \frac{1}{\mathcal{H}^2(\omega_\delta)} \int_{\omega_\delta} w_h \cdot z \,\mathrm{d}s.$$

Combining this identity to Proposition 3.1 yields

$$\left| \int_{\partial\Omega_{\mathrm{N}}} p_\delta \cdot h \,\mathrm{d}s \right| \leqslant \|z\| \|w_h\|_{C(\overline{\Omega}_0)} \leqslant C' \|z\| \|w_h\|_{W^{1,q}(\Omega_0)} \leqslant C'' \|z\| \|h\|_{L^q(\partial\Omega_{\mathrm{N}})},$$

where the constants C' and C'' are independent from δ (and from y). This means that $(p_\delta)_{\delta>0}$ is bounded as a family in $L^{q'}(\partial\Omega_{\mathrm{N}})$. One can thus extract from $(p_\delta|_{\partial\Omega_{\mathrm{N}}})_{\delta>0}$ a subsequence $(p_k)_{k\in\mathbb{N}}$ converging to some $p^* \in L^{q'}(\partial\Omega_{\mathrm{N}})$ for the weak-topology of $L^{q'}(\partial\Omega_{\mathrm{N}})$. Since

$$\lim_{\delta\searrow 0} \frac{1}{\mathcal{H}^2(\omega_\delta)} \int_{\omega_\delta} w_h \cdot z \,\mathrm{d}s = w_h(x_y) \cdot z,$$

we conclude that $p_{\ell,y} = p^*$ is a solution to (11). Now, if we define $p_\ell = \int_\Gamma p_{\ell,y} \,\mathrm{d}y$, we can use the Tonelli and Fubini theorems [5, Theorems IV.4 and IV.5] to check that

$$\forall h \in L^q(\partial\Omega_{\mathrm{N}}) \quad \int_{\partial\Omega_{\mathrm{N}}} p_\ell \cdot h \,\mathrm{d}s = \int_\Gamma \int_{\partial\Omega_{\mathrm{N}}} p_{\ell,y} \cdot h \,\mathrm{d}s \,\mathrm{d}y = \int_\Gamma w_h(x_y) \cdot (x_y + u(x_y) - y) \,\mathrm{d}y,$$

which makes p_ℓ a solution to the considered PDE.

Finally, regarding the uniqueness, one easily gets that if p_1 and p_2 are two solutions of the PDE, then

$$\int_{\partial\Omega_{\mathrm{N}}} (p_1 - p_2) \cdot h \, \mathrm{d}s = 0$$

for all $h \in L^q(\partial\Omega_{\mathrm{N}})$, hence the result.

A.4 Proof of Theorem 3.2

We first give a justification for the structure of $\mathrm{d}\Phi(g)$. For a direction $h \in L^\infty(\partial\Omega_{\mathrm{N}})$, we consider the associated displacement field perturbation w_h , which satisfies

$$\forall v \in H^1_{\mathrm{D}}(\Omega) \quad \int_{\Omega_0} A\varepsilon(w) : \varepsilon(v) \, \mathrm{d}x = \int_{\partial\Omega_{\mathrm{N}}} h \cdot v \, \mathrm{d}s.$$

By exploiting the notion of solution in the sense of transposition for Problem (6), we obtain for $\ell \in L(u)$

$$\langle \ell, w_h \rangle = \int_{\partial\Omega_{\mathrm{N}}} p_\ell \cdot h \, \mathrm{d}s,$$

hence

$$\mathrm{d}\Phi(g)(h) = \min_{\ell \in L(u)} \int_{\partial\Omega_{\mathrm{N}}} p_\ell \cdot h \, \mathrm{d}s.$$

We now characterize the cone of admissible directions at g. Let us introduce the active set $\mathcal{A}_g = \{x \in \partial\Omega_{\mathrm{N}} \mid \|g(x)\| = M\}$. The cone of admissible directions is the intersection $L^\infty(\partial\Omega_{\mathrm{N}}) \cap K$, where K is the closed cone

$$K = \left\{ h \in L^2(\partial\Omega_{\mathrm{N}}) \;\middle|\; \forall \lambda \in L^2(\partial\Omega_{\mathrm{N}}, \mathbb{R}_+) \quad \int_{\mathcal{A}_g} \lambda (h \cdot g) \, \mathrm{d}s \leqslant 0 \right\},$$

while its polar cone reads

$$Q = \left\{ \mathbf{1}_{\mathcal{A}_g} \lambda g, \lambda \in L^2(\partial\Omega_{\mathrm{N}}, \mathbb{R}_+) \right\}.$$

We denote by $-p_\ell = -p_K - p_Q$ the so-called *Moreau decomposition* of $-p_\ell$ [32] with $-p_K \in K$, $-p_Q \in Q$ and $\langle p_K, p_Q \rangle = 0$.

Now, the Euler inequation stipulates that $\mathrm{d}\Phi(g)(h) \geq 0$ for every element h of the cone of admissible directions. To derive the first-order optimality condition, we consider the admissible direction

$$h = \frac{p_K}{\max(1, \|p_K\|)} \in L^\infty(\partial\Omega_{\mathrm{N}}) \cap K.$$

As g is a local minimizer, it results from the Euler inequation that

$$0 \leqslant \mathrm{d}\Phi(g)(h) \leqslant \int_{\partial\Omega_{\mathrm{N}}} p_\ell \cdot h \, \mathrm{d}s = - \int_{\partial\Omega_{\mathrm{N}}} \min\left(\|p_K\|, \|p_K\|^2 \right) \mathrm{d}s.$$

Finally, we obtain $p_K(\cdot) = 0$, which yields the first-order optimality condition $p_\ell - p_Q = 0$. Observing that this condition rewrites as in the statement of Theorem 3.2, we are done.

References

[1] Robert A. Adams and John J. F. Fournier. *Sobolev spaces*, volume 140 of *Pure and Applied Mathematics (Amsterdam)*. Elsevier/Academic Press, Amsterdam, second edition, 2003.

[2] Jérémie Allard, Stéphane Cotin, François Faure, Pierre-Jean Bensoussan, François Poyer, Christian Duriez, Hervé Delingette, and Laurent Grisoni. SOFA - an Open Source Framework for Medical Simulation. In *MMVR 15 - Medicine Meets Virtual Reality*, volume 125 of *Studies in Health Technology and Informatics*, pages 13–18, Palm Beach, United States, February 2007. IOP Press.

[3] Paul J. Besl and Neil D. McKay. Method for registration of 3-D shapes. In Paul S. Schenker, editor, *Sensor Fusion IV: Control Paradigms and Data Structures*, volume 1611, pages 586 – 606. International Society for Optics and Photonics, SPIE, 1992.

[4] E. Lee Brewer, Logan W. Clements, Jarrod A. Collins, Derek J. Doss, Jon S. Heiselman, Michael I. Miga, Chris D. Pavas, and Edward H. Wisdom III. The image-to-physical liver registration sparse data challenge. In Baowei Fei and Cristian A. Linte, editors, *Medical Imaging 2019: Image-Guided Procedures, Robotic Interventions, and Modeling*, volume 10951, pages 364 – 370. International Society for Optics and Photonics, SPIE, 2019.

[5] Haïm Brezis. *Analyse fonctionnelle*. Collection Mathématiques Appliquées pour la Maîtrise. [Collection of Applied Mathematics for the Master's Degree]. Masson, Paris, 1983. Théorie et applications. [Theory and applications].

[6] Richard H. Byrd, Peihuang Lu, Jorge Nocedal, and Ciyou Zhu. A limited memory algorithm for bound constrained optimization. *SIAM Journal on Scientific Computing*, 16(5):1190–1208, 1995.

[7] Philippe G. Ciarlet. *Mathematical elasticity. Vol. I*, volume 20 of *Studies in Mathematics and its Applications*. North-Holland Publishing Co., Amsterdam, 1988. Three-dimensional elasticity.

[8] Jarrod A. Collins, Jared A. Weis, Jon S. Heiselman, Logan W. Clements, Amber L. Simpson, William R. Jarnagin, and Michael I. Miga. Improving registration robustness for image-guided liver surgery in a novel human-to-phantom data framework. *IEEE Transactions on Medical Imaging*, 36(7):1502–1510, 2017.

[9] H. Courtecuisse, Z. Jiang, O. Mayeur, J. F. Witz, P. Lecomte-Grosbras, M. Cosson, M. Brieu, and S. Cotin. Three-dimensional physics-based registration of pelvic system using 2d dynamic magnetic resonance imaging slices. *Strain*, 56(3):e12339, 2020.

[10] John M. Danskin. *The theory of max-min and its application to weapons allocation problems*. Econometrics and Operations Research, Vol. V. Springer-Verlag New York, Inc., New York, 1967.

[11] Maya de Buhan, Charles Dapogny, Pascal Frey, and Chiara Nardoni. An optimization method for elastic shape matching. *C. R. Math. Acad. Sci. Paris*, 354(8):783–787, 2016.

[12] Karoline Disser, Hans-Christoph Kaiser, and Joachim Rehberg. Optimal sobolev regularity for linear second-order divergence elliptic operators occurring in real-world problems. *SIAM Journal on Mathematical Analysis*, 47(3):1719–1746, 2015.

[13] Jérôme Droniou. Solving convection-diffusion equations with mixed, Neumann and Fourier boundary conditions and measures as data, by a duality method. *Adv. Differential Equations*, 5(10-12):1341–1396, 2000.

[14] Lawrence C. Evans. *Partial differential equations*, volume 19 of *Graduate Studies in Mathematics*. American Mathematical Society, Providence, RI, second edition, 2010.

[15] J. C. Gelin and P. Picart. Use of quasi-newton methods for large strain elastic-plastic finite element computations. *Communications in Applied Numerical Methods*, 4(4):457–469, 1988.

[16] Konrad Gröger. A $W^{1,p}$-estimate for solutions to mixed boundary value problems for second order elliptic differential equations. *Math. Ann.*, 283(4):679–687, 1989.

[17] Konrad Gröger and Joachim Rehberg. Resolvent estimates in $W^{-1,p}$ for second order elliptic differential operators in case of mixed boundary conditions. *Math. Ann.*, 285(1):105–113, 1989.

[18] Christian Gross and Rolf Krause. On the convergence of recursive trust-region methods for multiscale nonlinear optimization and applications to nonlinear mechanics. *SIAM Journal on Numerical Analysis*, 47(4):3044–3069, 2009.

[19] Antonin Guttman. R-trees: A dynamic index structure for spatial searching. *SIGMOD Rec.*, 14(2):47–57, June 1984.

[20] R. Haller-Dintelmann, C. Meyer, J. Rehberg, and A. Schiela. Hölder continuity and optimal control for nonsmooth elliptic problems. *Appl. Math. Optim.*, 60(3):397–428, 2009.

[21] N. Haouchine, S. Cotin, I. Peterlík, J. Dequidt, M. S. Lopez, E. Kerrien, and M. Berger. Impact of soft tissue heterogeneity on augmented reality for liver surgery. *IEEE Transactions on Visualization and Computer Graphics*, 21(5):584–597, 2015.

[22] N. Haouchine, J. Dequidt, I. Peterlík, E. Kerrien, M. Berger, and S. Cotin. Image-guided simulation of heterogeneous tissue deformation for augmented reality during hepatic surgery. In *2013 IEEE International Symposium on Mixed and Augmented Reality (ISMAR)*, pages 199–208, 2013.

[23] Jon S. Heiselman, Logan W. Clements, Jarrod A. Collins, Jared A. Weis, Amber L. Simpson, Sunil K. Geevarghese, T. Peter Kingham, William R. Jarnagin, and Michael I. Miga. Characterization and correction of intraoperative soft tissue deformation in image-guided laparoscopic liver surgery. *Journal of Medical Imaging*, 5(2):1 – 12, 2017.

[24] Jon S. Heiselman, William R. Jarnagin, and Michael I. Miga. Intraoperative correction of liver deformation using sparse surface and vascular features via linearized iterative boundary reconstruction. *IEEE Transactions on Medical Imaging*, 39(6):2223–2234, 2020.

[25] Roland Herzog, Christian Meyer, and Gerd Wachsmuth. Integrability of displacement and stresses in linear and nonlinear elasticity with mixed boundary conditions. *J. Math. Anal. Appl.*, 382(2):802–813, 2011.

[26] K. Krumbiegel and J. Rehberg. Second order sufficient optimality conditions for parabolic optimal control problems with pointwise state constraints. *SIAM Journal on Control and Optimization*, 51(1):304–331, 2013.

[27] W. Littman, G. Stampacchia, and H. F. Weinberger. Regular points for elliptic equations with discontinuous coefficients. *Ann. Scuola Norm. Sup. Pisa Cl. Sci. (3)*, 17:43–77, 1963.

[28] Stéphanie Marchesseau, Simon Chatelin, and Hervé Delingette. Nonlinear biomechanical model of the liver. In Yohan Payan and Jacques Ohayon, editors, *Biomechanics of Living Organs*, volume 1 of *Translational Epigenetics*, pages 243–265. Academic Press, Oxford, 2017.

[29] Guillaume Mestdagh. *An optimal control formulation for organ registration in augmented surgery*. Theses, Université de Strasbourg, December 2022.

[30] Guillaume Mestdagh and Stéphane Cotin. An optimal control problem for elastic registration and force estimation in augmented surgery. In Linwei Wang, Qi Dou, P. Thomas Fletcher, Stefanie Speidel, and Shuo Li, editors, *Medical Image Computing and Computer Assisted Intervention – MICCAI 2022*, pages 74–83, Cham, 2022. Springer Nature Switzerland.

[31] Karol Miller, Grand Joldes, Dane Lance, and Adam Wittek. Total lagrangian explicit dynamics finite element algorithm for computing soft tissue deformation. *Communications in Numerical Methods in Engineering*, 23(2):121–134, 2007.

[32] Jean Jacques Moreau. Décomposition orthogonale d'un espace hilbertien selon deux cônes mutuellement polaires. *Comptes rendus hebdomadaires des séances de l'Académie des sciences*, 255:238–240, 1962.

[33] Fanny Morin, Hadrien Courtecuisse, Ingerid Reinertsen, Florian Le Lann, Olivier Palombi, Yohan Payan, and Matthieu Chabanas. Brain-shift compensation using intraoperative ultrasound and constraint-based biomechanical simulation. *Medical image analysis*, 40:133–153, 2017.

[34] Chiara Nardoni. *Mesh deformation strategies in shape optimization. Application to forensic facial reconstruction*. Theses, Université Pierre et Marie Curie - Paris VI, October 2017.

[35] Matthieu Nesme, Yohan Payan, and François Faure. Efficient, Physically Plausible Finite Elements. In *Eurographics*, Short papers, Dublin, Ireland, August 2005.

[36] Sergei Nikolaev and Stéphane Cotin. Estimation of boundary conditions for patient-specific liver simulation during augmented surgery. *International Journal of Computer Assisted Radiology and Surgery*, 15(7):1107–1115, May 2020.

[37] Alban Odot, Guillaume Mestdagh, Yannick Privat, and Stéphane Cotin. Real-time elastic partial shape matching using a neural network-based adjoint method. Preprint: https://hal.inria.fr/hal-04019777v1, March 2023.

[38] Rogelio Ortigosa, Jesus Martínez-Frutos, Carlos Mora-Corral, Pablo Pedregal, and Francisco Periago. Optimal control of soft materials using a Hausdorff distance functional. *SIAM Journal on Control and Optimization*, 2020.

[39] Erol Özgür, Bongjin Koo, Bertrand Le Roy, Emmanuel Buc, and Adrien Bartoli. Preoperative liver registration for augmented monocular laparoscopy using backward–forward biomechanical simulation. *International Journal of Computer Assisted Radiology and Surgery*, 13(10):1629–1640, October 2018.

[40] Ece Ozkan and Orcun Goksel. Compliance boundary conditions for patient-specific deformation simulation using the finite element method. *Biomedical Physics & Engineering Express*, 4(2):025003, January 2018.

[41] Igor Peterlík, Hadrien Courtecuisse, Robert Rohling, Purang Abolmaesumi, Christopher Nguan, Stéphane Cotin, and Septimiu Salcudean. Fast elastic registration of soft tissues under large deformations. *Medical Image Analysis*, 45:24–40, 2018.

[42] Igor Peterlík, Christian Duriez, and Stéphane Cotin. Modeling and real-time simulation of a vascularized liver tissue. In Nicholas Ayache, Hervé Delingette, Polina Golland, and Kensaku Mori, editors, *Medical Image Computing and Computer-Assisted Intervention – MICCAI 2012*, pages 50–57, Berlin, Heidelberg, 2012. Springer Berlin Heidelberg.

[43] Rosalie Plantefève, Igor Peterlík, Nazim Haouchine, and Stéphane Cotin. Patient-specific biomechanical modeling for guidance during minimally-invasive hepatic surgery. *Annals of Biomedical Engineering*, 44(1):139–153, January 2016.

[44] Augusto C. Ponce. *Elliptic PDEs, measures and capacities*, volume 23 of *EMS Tracts in Mathematics*. European Mathematical Society (EMS), Zürich, 2016. From the Poisson equations to nonlinear Thomas-Fermi problems.

[45] D. Caleb Rucker, Yifei Wu, Logan W. Clements, Janet E. Ondrake, Thomas S. Pheiffer, Amber L. Simpson, William R. Jarnagin, and Michael I. Miga. A mechanics-based nonrigid registration method for liver surgery using sparse intraoperative data. *IEEE Transactions on Medical Imaging*, 33(1):147–158, 2014.

[46] Peter Shi and Steve Wright. Higher integrability of the gradient in linear elasticity. *Math. Ann.*, 299(3):435–448, 1994.

[47] Aristeidis Sotiras, Christos Davatzikos, and Nikos Paragios. Deformable medical image registration: A survey. *IEEE transactions on medical imaging*, 32(7):1153, 2013.

[48] Stefan Suwelack, Sebastian Röhl, Sebastian Bodenstedt, Daniel Reichard, Rüdiger Dillmann, Thiago dos Santos, Lena Maier-Hein, Martin Wagner, Josephine Wünscher, Hannes Kenngott, Beat P. Müller, and Stefanie Speidel. Physics-based shape matching for intraoperative image guidance. *Medical Physics*, 41(11):111901, 2014.

[49] Hujin Xie, Jialu Song, Yongmin Zhong, Chengfan Gu, and Kup-Sze Choi. Constrained finite element method for runtime modeling of soft tissue deformation. *Applied Mathematical Modelling*, 109:599–612, 2022.

[50] Jonathan Youett, Oliver Sander, and Ralf Kornhuber. A globally convergent filter-trust-region method for large deformation contact problems. *SIAM Journal on Scientific Computing*, 41(1):B114–B138, 2019.

[51] Yasunori Yusa, Shota Miyauchi, and Hiroshi Okada. Performance investigation of quasi-newton-based parallel nonlinear fem for large-deformation elastic-plastic analysis over 100 thousand degrees of freedom. *Mechanical Engineering Journal*, 8(3):21–00053–21–00053, 2021.